Analysis of failure modes in three-dimensional woven composites subjected to quasi-static indentation

Prabhakar M Rao, Timothy R Walter, Bhavani Sankar, Ghatu Subhash and Chian F Yen

Journal of Composite Materials 2014 48: 2473 originally published online 9 September 2013
DOI: 10.1177/0021998313499950

Article

JOURNAL OF COMPOSITE MATERIALS

Journal of Composite Materials
2014, Vol. 48(20) 2473–2491

DOI: 10.1177/0021998313499950
jcm.sagepub.com
SAGE

Analysis of failure modes in three-dimensional woven composites subjected to quasi-static indentation

Prabhakar M Rao[1,*], Timothy R Walter[2], Bhavani Sankar[2], Ghatu Subhash[2] and Chian F Yen[3]

Abstract

Finite element models are developed to predict potential failure initiation sites and associated failure modes in S2-Glass/SC15 three-dimensional (3D) woven composites under quasi-static indentation. As part of this modeling effort, experimental micrographs of the composite specimen obtained from a previous experimental study[1,2] are analyzed. In conjunction with these micrographs, model outcomes demonstrate the ability of warp weavers or through-thickness Z-yarns to shield inter-laminar cracks. Quasi-static indentation is modeled as a contact interaction between a rigid cylindrical indenter and a deformable S2-Glass/SC15 3D woven composite laminate using ABAQUS®. Tow elements are modeled as transversely isotropic elastic-plastic material entities, whereas the inter-tow matrix is modeled as an isotropic elastic-plastic material. Through-thickness failure modes are predicted based on the Tsai-Hill criterion. Contour maps of these failure modes point to the location and corresponding damage initiation mode within the material. Experimentally obtained micrographs[1,2] are then analyzed on the basis of these contour maps, thereby serving to validate the modeling methodology. The effect of Z-yarns is demonstrated with the aid of two-dimensional plane strain linear elastic fracture mechanics analysis. Crack shielding abilities of the Z-yarns manifest as the variation of strain energy release rate as a function of crack length and location. In the vicinity of a Z-yarn, the energy release rate decreases precipitously, indicating the inability of the crack to penetrate the Z-yarns.

Keywords

3D Woven composites, indentation mechanics, anisotropic yielding, failure modes, delamination cracking

Introduction

Designing composite structures that will perform satisfactorily under impact loads is an exceedingly challenging problem. Current research focusses on exploring the application of advanced materials to design and fabricate inhomogeneous, light-weight, and cost-effective structures that have good impact damage tolerance for various applications. Inhomogeneous construction herein implies the inclusion of different materials that together effectively dissipate the energy of the impacting projectiles. In such systems, integrally woven three-dimensional (3D) fabric composites are being increasingly applied to construct structural members. From a micro-structural geometry perspective, 3D woven composites comprise of several layers of 0/90 laminas integrally woven with through-thickness reinforcements known as warp-weavers or Z-yarns. Herein, the focus is on 3D woven composites with architectures similar to those reported in recent works.[1–9]

These materials have been studied by many researchers over the past two decades or more, notably by Cox et al.[10–15] The subjects of investigation in their studies have included buckling of delaminated layers in 3D composites,[10] effective elastic properties of 3D composites accounting for geometrical irregularities such as tow waviness,[11] and work of fracture in 3D woven composites under tensile loading.[12] A computationally

[1]Solid Mechanics Group, Physical Sciences Department, United Technologies Research Center, East Hartford, CT, USA
[2]Department of Mechanical & Aerospace Engineering, University of Florida, Gainesville, FL, USA
[3]U.S. Army Research Laboratory, 4600 Deer Creek Loop, Aberdeen Proving Ground, MD, USA

*This work was performed while the author was a Post-Doctoral Research Associate at the Department of Mechanical & Aerospace Engineering, University of Florida, Gainesville, FL 32611

Corresponding author:
Prabhakar M Rao, Solid Mechanics Group, Physical Sciences Department, United Technologies Research Center, 411 Silver Lane, MS 129-73, East Hartford, CT 06108, USA.
Email: raomp@utrc.utc.com

efficient Binary Model was developed by Cox et al.,[13] which was subsequently applied by Xu et al.[14] to study the elastic response of 3D composites. The weave architecture in 3D angle interlock composites was shown to influence the fracture toughness via the lockup mechanism based on geometrically enhanced friction.[15]

However, incorporation of 3D woven composites in hierarchical impact protection systems necessitates complete mechanical characterization of these materials under through-thickness quasi-static, dynamic, and impact loads. The key parameter of interest, therefore, manifests as the role of Z-yarns within the purview of the aforementioned loading environments. The approach taken herein is based on developing finite element models of quasi-static indentation of 3D woven composites mimicking the short-beam shear experiments of Walter et al.[1,2] Stress states in material planes comprising the Z-yarns and in between two consecutive Z-yarns are analyzed. As will be discussed in later sections, these results reveal the presence of a zone of high inter-laminar shear stress, consistent with the studies of Walter et al.[3] The failure modes contour maps developed on the basis of the above analysis predict potential sites of inter-laminar delaminations, which correlate reasonably well with experimental evidence, thereby lending credibility to the developed model. This work differs from previous studies[6–17] which focused primarily on the in-plane tensile response of 3D woven composites.

More recently, Pankow et al.[4,5] introduced an edge crack in 3D woven composite specimens to perform quasi-static and low-rate indentation tests in the End Notch Flexure (ENF) configuration with the objective of discerning the effects of weave architecture. It was shown that the architecture with Z-yarn reinforcement enhanced strength at the quasi-static loading rates, whereas the layer-to-layer reinforcement provided better energy absorption by preventing Mode II crack propagation.[4] As such, the present work, based on the experimental investigations of Walter et al.[1–3] fundamentally differs from that of Pankow et al.[4,5] since a pre-crack is not introduced. Rather, the endeavor herein is to capture the effects of the weave architecture in an as-fabricated condition.

Analytical and computational studies[6,9,16,17] have predominantly addressed estimation of effective properties and in-plane failure strengths of 3D woven composites. In general, the aforementioned studies show that through-thickness Z-yarns are detrimental to the planar stiffness and strength of 3D woven composite laminates.

Through-thickness mechanics of 3D woven composites under quasi-static perforation has been reported in Gama et al.[18] and Baucom and Zikry[19] Performing quasi-static punch shear simulations, Gama et al.[18] showed that 3D woven composite panels in general have better energy transfer characteristics. Baucom and Zikry[19] experimentally showed that 3D woven composite laminates have better damage tolerance characteristics relative to two-dimensional (2D) woven and 3D monolithic composite laminates. Interestingly, Baucom and Zikry[19] point out that 3D woven composite laminates exhibit better damage tolerance due to particular energy absorption mechanisms involving the 'Z-Crowns'.[6,9]

Dynamic through-thickness mechanics, on the other hand, have been addressed in computational investigations reported in Bahei-El-Din and Zikry[20] and Lv and Gu[21] and in experimental studies by Grogan et al.[22] and Gong and Sankar.[23] Bahei-El-Din and Zikry[20] showed that at low velocities of impact, damage in 3D woven composites resembles failure in quasi-static three-point bending, whereas at high velocities wave propagation effects dictate localized failure in the vicinity of the indenter. Lv and Gu[21] and Grogan et al.[22] compared 2D and 3D woven composites and determined the superiority of the latter in improving ballistic efficiency and resistance to delamination. While studies by Gama et al.[18] accounted for most details of the weave architecture, Bahei-El-Din and Zikry[20] and Lv and Gu[21] completely homogenized the micro-structure, thereby rendering the isolation of the effects of Z-yarns under impact loading somewhat difficult.

Matrix cracking, separation of fiber tows and tow breakage were identified as the chief damage mechanisms by Gong and Sankar.[23] The extents of the observed damage therein[23] were reported to be more severe from a low mass high velocity projectile, than a high mass low velocity projectile, since energy, $E \propto V_p^2$, wherein, V_p is the projectile velocity. It was also shown therein[23] that the woven architecture aids the damage tolerance as it provides an effective containment of the propagation of damage.

Recent studies have also reported on impact[24,25] and rate-dependent response[26] of 3D woven composites. Herb et al.[24] reported that primary damage mechanisms such as fiber bundle and matrix cracking remained local to the vicinity of impact in SiC/SiC 3D woven composites. Seltzer et al.[25] on the other hand reported that Z-yarn reinforcements imparted superior energy absorption traits to S2-Glass/SC15 3D woven composites by delaying delamination, thereby promoting and maintaining the structural integrity of the material system. Pankow et al.[26] showed that 3D woven composites are also characterized by transitions in failure modes, which range from kink band formation at low-rates to delaminations at high-rates of compressive loading.

The above cited body of work represents rigorous experimental and computational investigations into the various mechanical aspects of 3D woven composite systems. The critical parameters involved were shown to include the effects of weave architecture,

determination of the effective elastic properties and strengths, failure behavior,[1–17] and the assessment of the role of the type of projectile on the through-thickness mechanics of 3D woven composites under quasi-static, dynamic, and impact loading conditions.[18–23]

Consistent with the historical direction of research in 3D woven composites, this work endeavors to investigate the effect of weave architecture under quasi-static indentation. Based on the computed stress states, zones of high inter-laminar shear stress are predicted. These stress results are incorporated into a Tsai-Hill criterion centered model to determine potential failure modes. Information regarding failure modes is presented as contour maps, which bring to light potential regions of extensive inter-laminar delamination. This evidence is used to construct 2D linear elastic fracture mechanics (LEFM) models, wherein an inter-laminar crack is grown incrementally. In the vicinity of a Z-yarn, the strain energy release rate ($\mathcal{G}$) decreases precipitously, whereas such an effect is absent in the regions between two consecutive Z-yarns. These outcomes might help explain the findings of Seltzer et al.[25] wherein Z-yarns were attributed for maintaining the structural integrity of the 3D woven composite system.

Finite element modeling of quasi-static indentation

Statement of the problem

Quasi-static indentation of 3D woven composites is modeled as a contact interaction problem, schematically illustrated in Figure 1. The commercially available ABAQUS® finite element software is used to cast the problem illustrated in Figure 1 in a computational framework. The built-in surface-to-surface contact algorithm[27] is used to define contact conditions between the rigid circular indenter and support rollers and the deformable 3D woven composite laminate. The indenter is displaced downwards by specifying $U_z = 1.5\,\text{mm}$ as a ramp input in steps of $\delta U_z = 0.05\,\text{mm}$, in order to adequately capture the progression of the solution.

As will be discussed later, experiments performed by Walter et al.[1] indicate that the indenter displacement of $U_z = 1.5\,\text{mm}$ includes the linear elastic, softening, and damage-induced nonlinear response of the 3D woven composites studied herein. As such, this study endeavors to understand the role of the 3D weave architecture in the above regimes of the mechanical response.

Characterizing the geometry of 3D woven composite panels

Figure 2 shows micrographs and schematic representations of a particular class of orthogonal interlock[16] 3D woven composites. Figure 2(a) shows the micrographs[1] of the 3D woven composite laminates arranged in 3D space such that the weave architecture becomes apparent.

A dent is defined as the space between two adjacent columns of fill tows in a 3D woven fabric.[9] Through every such dent in the X–Y plane, two Z-yarns traverse

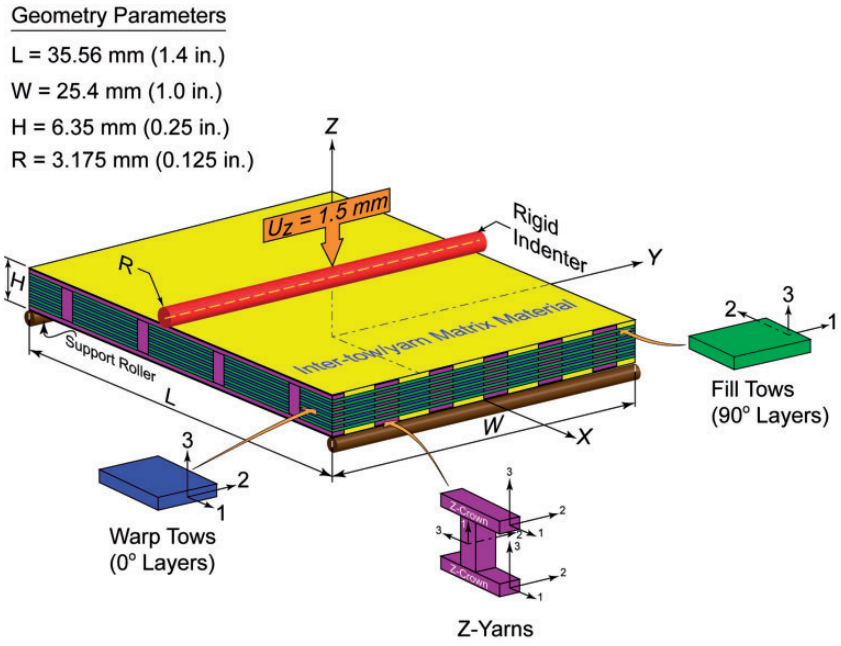

Figure 1. Schematic representation of quasi-static indentation problem modeled in this work.

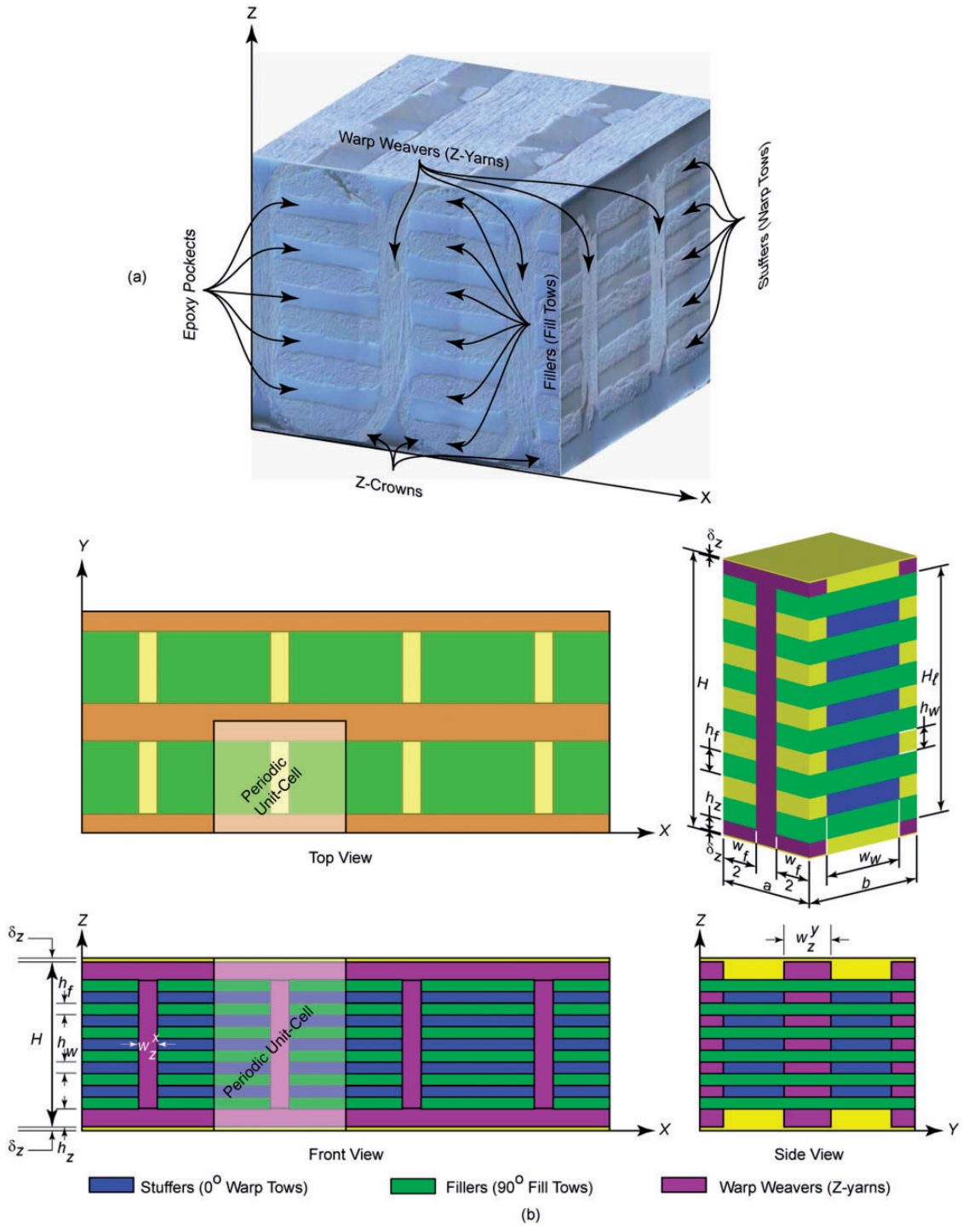

Figure 2. Weave architecture of 3D woven composite laminates. (a) Sectional micrographs of the 3D woven composite panels arranged in a cube to illustrate internal geometric details.[1] (b) Idealized schematics reconstructed on the basis of the sectional micrographs of 3D woven composites and the solid model of the corresponding unit-cell.

the thickness direction of the 3D fabric composite, as shown in Figure 2(a). This material system is therefore designated as the Double Stitched 3D Woven Composite in this study. As a result, this weave pattern is characterized by two Z-Crowns[6,9] near the top and bottom as shown in Figure 2(a). Z-Crowns are the crimped segments of the Z-yarns, which soften the elastic response due to micro-bending,[6] but are involved in unique energy transfer mechanisms leading to better damage tolerance in 3D woven composites.[19]

While the surface fill tows in contact with the Z-Crowns attain semi-circular cross-sections, the internal fill tows and all of the warp tows are characterized by nominally rectangular cross-sections. Furthermore, examination of several micrographs complementary to the ones shown in Figure 2(a) revealed that the inter-tow volume within the Double Stitched 3D Woven Composite panels was occupied by the SC-15 epoxy matrix material and some discrete porosity manifesting as large-scale voids. The Army Research Laboratory estimated the porosity volume fraction as approximately 2.8% of the overall volume to tested specimens. However, in this study effects of porosity are neglected.

The complex geometry of the material system represented in Figure 2(a) is idealized as shown in Figure 2(b). Notably in Figure 2(b), the Z-Crowns have been flattened and the semi-circular cross-sections of the surface fill tows have been replaced with rectangular ones. Tows in textile composites have been modeled with rectangular cross-sections, as reported in the exhaustive review paper by Ansar et al.[28] Also, the two distinct Z-yarns in Figure 2(a) are modeled herein as a single entity. Modeling the double Z-yarns in the through-thickness direction as a single entity is admissible since the 1-directions of these Z-yarns are parallel to each other. Therefore, an advancing model crack will meet with the same resistance to propagation, whether the through-thickness Z-yarns are modeled as double or single entities. In addition, overall confinement will be provided by the Z-Crowns which are modeled as 0°-oriented tows in this work. The geometry parameters introduced to model the architecture are listed in Figure 2(b). The tow and yarn cross-sectional dimensions are superimposed on the 3D micrograph[1] as shown in Figure 2(a).

The idealization of the weave architecture is built upon the requirement of keeping the overall volume fraction of Z-yarns in the model consistent with their volume fraction in the experimental specimen. Herein, the volume fraction of the Z-yarns is $v_{ZYarns}^{Specimen} = 0.1$ in the fabricated specimen. As shown in Figure 2(a), the Z-Crowns are curved and correspondingly the fill tows in contact with the Z-Crowns attain a cross-section shape that could be construed as a semi-circular arc on top of a rectangle. While making modifications to the Z-Crown regions in the model, the above cross-sectional geometry of the fill tows was replaced with an equivalent rectangle and the path of the Z-yarns was also accordingly updated, as shown in Figure 2(b). In doing so, the overall height of the model specimen and the height (or thickness) of the warp tows, h_w, were also maintained consistent with those in the fabricated specimen. Upon interrogating element volumes in ABAQUS, the following magnitudes are reported for individual constituents: $V_{\mathrm{FillTows}} = 602.17\,\mathrm{mm}^3$, $V_{\mathrm{WarpTows}} = 414.11\,\mathrm{mm}^3$, $V_{\mathrm{ZYarns}} = 174.74\,\mathrm{mm}^3$ and $V_{\mathrm{Matrix}} = 400.74\,\mathrm{mm}^3$. Based on the above data, the total volume computed as the sum of the constituent volumes is $V_{\mathrm{Total}} = 1591.76\,\mathrm{mm}^3$. Therefore, the volume fraction of the Z-Yarns in the model is computed as: $v_{ZYarns}^{Model} = \frac{V_{\mathrm{ZYarns}}}{V_{Total}} = 0.11$. It is evident that the volume fraction of Z-Yarns in the model is consistent with the fabricated specimen.

The as-fabricated specimens of the 3D composites studied herein indicated that the SC15 matrix completely surrounded the woven fibers, forming thin slivers on all sides. In order to eschew numerical instabilities these thin slivers of SC15 are not included in the models. As a result, the weave architecture becomes visible, as shown in Figures 1 and 2.

Meshing and boundary conditions

Due to symmetry only a quarter of the configuration shown in Figure 1 is modeled in this study. Schematic and finite element models of the quarter-symmetric quasi-static indentation problem are illustrated in Figure 3. The analyses performed in this study endeavor to predict various modes of failure and corresponding modes of damage. The objective herein is not to capture damage progression, but rather to shed light on potential damage mechanisms. The predicted stress states are employed to discern the most likely sites of failure initiation, and the corresponding failure and damage modes.

The right circular indenter and the support rollers are modeled as analytical rigid surfaces. The finite element mesh of the Double Stitched 3D Woven Composite plate is discretized with 3D 8-noded reduced integration linear continuum brick elements. In particular, a biased structured meshing scheme is used. The bias was set such that a finer mesh was achieved within the contact zone in the vicinity of the indenter, and a coarser mesh was deemed suitable away from the same. The length of the contact zone was determined as discussed elsewhere.[7] Overall, the meshing strategy was designed such that either very slender or very wide plate-like elements were not generated. Particular care was taken to ensure that sufficient elements were in contact with the indenter as well as the support rollers. The quarter-symmetric finite element mesh comprised of 175,505 nodes and 142,970 elements resulting in a total of 451,929 degrees of freedom.

Symmetry, displacement, and support boundary conditions listed in Table 1 are appropriately imposed on the finite element mesh. Contact conditions between the Double Stitched 3D Woven Composite specimen and the support roller and the support boundary conditions on reference point RP2 (see Figure 3) prevent any rigid body motion.

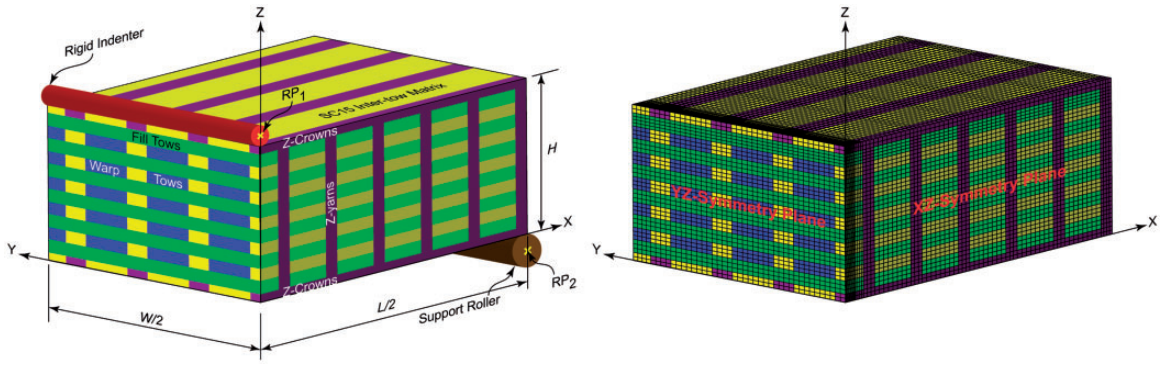

Figure 3. (a) Quarter symmetric solid model of the short beam shear configuration shown in Figure 1. (b) 3D finite element model of the short-beam shear specimen shown in Figure 1.

Table 1. Symmetry, displacement, and support boundary conditions specified to simulate quasi-static indentation of the three material systems investigated in this study.

Boundary conditions for quasi-static indentation						
Plane/edge	u_x	u_y	u_z	ϕ_x	ϕ_y	ϕ_z
XZ-symmetry	*Free*	*0*	*Free*	*NA*	*NA*	*NA*
YZ-symmetry	*0*	*Free*	*Free*	*NA*	*NA*	*NA*
Indenter – RP1	*0*	*0*	*−1.5*	*0*	*0*	*0*
Roller – RP2	*0*	*0*	*0*	*0*	*0*	*0*

Material models for fiber tows and matrix

The unidirectional warp and fill tows and the through-thickness Z-yarns are comprised of S2-Glass fibers embedded in an SC-15 epoxy resin matrix. As before, the inherent dispersed and discrete porosity is neglected. These S2-Glass/SC-15 tows and yarns are modeled as transversely isotropic elastic-plastic material entities. On the other hand, the SC-15 epoxy is modeled as an isotropic elastic-plastic material.

The S2-Glass fibers and the SC-15 epoxy are modeled as isotropic materials as indicated by their properties listed in [29, 30], respectively. The elastic modulus and Poisson's ratio of the S2-Glass fibers are taken to be $E_f = 88\,GPa$ and $\nu_f = 0.23$, respectively. The volume fraction of the S2-Glass fibers within the S2-Glass/SC-15 tows is assumed to be $V_f = 0.5$. Furthermore, the elastic modulus and Poisson's ratio of the SC-15 epoxy are set equal to $E_m = 2.5\,\text{GPa}$ and $\nu_m = 0.30$, respectively. Then the transversely isotropic effective elastic properties of the S2-Glass/SC-15 unidirectional tows and yarns are computed with the aid of the simplified micromechanics formulas presented by Chamis et al.[31] These properties are listed in Table 2.

The softening response of the S2-Glass/SC-15 tows is modeled using the Anisotropic Yielding Model (AYM) built into ABAQUS.[27] This model implements Hill's[32] 3D quadratic plastic potential function for anisotropic materials as:

$$f(\sigma) = \sqrt{\begin{array}{c} F(\sigma_{22}-\sigma_{33})^2 + G(\sigma_{33}-\sigma_{11})^2 + H(\sigma_{11}-\sigma_{22})^2 \\ +2L\sigma_{23}^2 + 2M\sigma_{31}^2 + 2N\sigma_{12}^2 \end{array}} \tag{1}$$

In equation (1), σ_{ij}, $i,j = 1,2,3$ are the stresses in the principal material directions and F, G, H, L, M, and N are constant plasticity parameters that depend on the current state of anisotropy.

Let us assume that $X, Y,$ and Z are the tensile strengths in the 1-, 2-, and 3-directions, respectively, and $R, S,$ and T are the shear strengths parallel to the 2-3, 3-1, and 1-2 planes, respectively. If σ_r is some user-defined reference stress, and $\tau_r = \sigma_r/\sqrt{3}$, then it is easily shown that

$$\begin{aligned} F &= \frac{\sigma_r^2}{2}\left[\frac{1}{Y^2}+\frac{1}{Z^2}-\frac{1}{X^2}\right] = \frac{1}{2}\left[\frac{1}{R_{22}^2}+\frac{1}{R_{33}^2}-\frac{1}{R_{11}^2}\right] \\ G &= \frac{\sigma_r^2}{2}\left[\frac{1}{Z^2}+\frac{1}{X^2}-\frac{1}{Y^2}\right] = \frac{1}{2}\left[\frac{1}{R_{33}^2}+\frac{1}{R_{11}^2}-\frac{1}{R_{22}^2}\right] \\ H &= \frac{\sigma_r^2}{2}\left[\frac{1}{X^2}+\frac{1}{Y^2}-\frac{1}{Z^2}\right] = \frac{1}{2}\left[\frac{1}{R_{11}^2}+\frac{1}{R_{22}^2}-\frac{1}{R_{33}^2}\right] \end{aligned} \tag{2}$$

Table 2. Properties of the SC-15 epoxy and unidirectional S2-Glass/SC-15 composites computed with the aid of Ref. 31.

Material properties of the SC-15 Epoxy – moduli in GPa and strength in MPa								
E_m		G_m		ν_m		σ_y^M		
2.50		0.96		0.30		12.50		
All elastic and shear moduli are reported in GPa								
E_{11}	E_{22}	E_{33}	ν_{12}	ν_{23}	ν_{13}	G_{12}	G_{23}	G_{13}
45.35	8.853	8.853	0.265	0.265	0.282	3.133	3.133	3.133
All strengths are reported in MPa								
S_L^+		S_L^-		S_T^+		S_T^-		S_{LT}
1380		770		47		137		50

Note: The reported strength values of unidirectional S2-Glass/SC-15 composites are referenced from [18].

and,

$$L = \frac{3}{2}\left(\frac{\tau_r}{R}\right)^2 = \frac{3}{2R_{23}^2}$$
$$M = \frac{3}{2}\left(\frac{\tau_r}{S}\right)^2 = \frac{3}{2R_{31}^2} \quad (3)$$
$$N = \frac{3}{2}\left(\frac{\tau_r}{T}\right)^2 = \frac{3}{2R_{12}^2}$$

As such, equations (2) and (3) define the plasticity parameters F, G, H, L, M, and N in terms of the anisotropic yield stress ratios R_{11}, R_{22}, R_{33}, R_{12}, R_{23}, and R_{31}.

Traditionally, the plasticity parameters are determined by performing several off-axis tests, for instance, as reported elsewhere[33]. Indeed, these parameters could also be determined via detailed micro-mechanical analysis as reported in the exhaustive study by Xie and Adams.[34] In their study, Xie and Adams[34] modeled S2-Glass/3501-6 unidirectional composites as transversely isotropic material entities. Beginning with Hill's[32] quadratic potential function, Xie and Adams[34] computed the above plasticity parameters for the S2-Glass/3501-6 unidirectional composites as $F = 0.3$, $G = 0.0$, $H = 0.0$, $L = 1.0$, $M = 1.4$, $N = 1.4$. Because of the transverse isotropy and linear behavior of unidirectional composites in the fiber direction (*1*-direction) until failure, the plasticity model is essentially reduced to a two-parameter model.

In the present study, it is assumed that the above plasticity parameters are also applicable to S2-Glass/SC-15 unidirectional composites. Using equations (2) and (3), and setting $G = H = 10^{-6}$ to avoid numerical singularities during matrix inversion while solving equation (2), the anisotropic yield stress ratios are then computed as: $R_{11} = 707.11$, $R_{22} = 1.83$, $R_{33} = 1.83$, $R_{12} = 1.45$, $R_{23} = 1.45$, and $R_{31} = 1.23$

From equation (2) it can be easily discerned that $R_{11} = X/\sigma_r$. Therefore, the high value of R_{11} implies that $X \gg \sigma_r$, further indicating that the unidirectional S2-Glass/SC-15 composite does not yield in the fiber- or *1*-direction. This result is consistent with the stated linear behavior of the unidirectional composite in the *1*-direction.[34] The other stress ratios above indicate that the unidirectional S2-Glass/SC-15 composite would yield when loaded in directions transverse (*2*- and *3*-) to the fiber direction. Further, pure shear loading of the unidirectional S2-Glass/SC-15 composite in planes parallel to the 1-2, 2-3, and 3-1 principal planes would also result in yielding, as indicated by the stress ratios computed above.

Xie and Adams[34] developed an empirical effective stress ($\bar{\sigma}$) – effective plastic strain ($\bar{\varepsilon}_p$) relation based on the micro-mechanical analyses of S2-Glass/3501-6 unidirectional composites, given as:

$$\bar{\sigma} = \frac{E\bar{\varepsilon}_p}{\left[1 + \left(\frac{E\bar{\varepsilon}_p}{\sigma_0}\right)^{n_1}\right]^{\frac{1}{n_1}}} \quad (4)$$

In equation (4), $E = 3310$ GPa, $\sigma_0 = 0.22$ GPa, and $n_1 = 0.44$ are curve-fitting parameters. It was shown in [34] that the $\bar{\sigma} - \bar{\varepsilon}_p$ relation in equation (4) adequately captures the complete non-linear behavior of S2-Glass/3501-6 unidirectional composites. It is assumed herein that the functional form of the $\bar{\sigma} - \bar{\varepsilon}_p$ relation in equation (4), shown in Figure 4(a), is also applicable to unidirectional S2-Glass/SC-15 composites.

Zhou et al.[35] characterized the complete non-linear behavior of the SC-15 epoxy at different strain rates. Assuming additive decomposition of the total strain into its elastic and inelastic components and that the inelastic strain rate could be represented as a power-law function of stress, Zhou et al.[35] proposed the following $\sigma - \varepsilon$ relation for the SC-15 epoxy:

$$\frac{d\sigma}{d\varepsilon} = E - E\left(\frac{\sigma}{\sigma^*}\right)^{n_2} \quad (5)$$

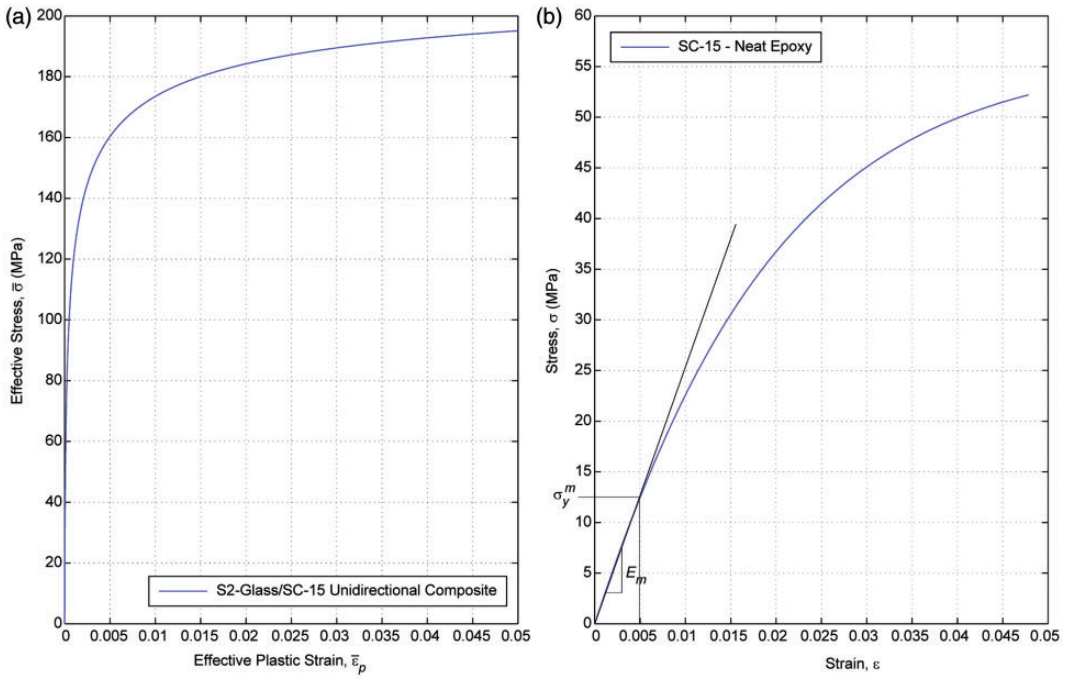

Figure 4. (a) The effective stress–effective plastic strain response of the unidirectional S2-Glass/SC-15 tows and yarns computed from equation (4) and based on the work of Xie and Adams.[34] (b) The $\sigma - \varepsilon$ response of the SC-15 neat epoxy computed from equation (5) and based on the work of Zhou et al.[35]

In equation (5), the stress coefficient $\sigma^* = \sigma_0 / \sqrt[n_2]{C/\dot{\varepsilon}}$, where σ_0 and n_2 are the reference stress and stress exponent, and C and $\dot{\varepsilon}$ are a material parameter and total strain rate, respectively. Zhou et al.[35] report extensive experimental studies to determine σ^* and n_2 as required by the fundamental constitutive relation in equation (5). The parameter $\sigma^* = 56.5\,\text{MPa}$ and $n_2 = 1.2$ for the SC15 neat epoxy.[35] The constitutive relation of equation (5) is presented in Figure 4(b). The values of σ^* and n_2 reported earlier are taken from [35] at a strain rate of $\dot{\varepsilon} = 0.00033\,s^{-1}$. This strain-rate is within the regime of quasi-static loading, and hence in this study any rate-dependent simulations are not performed.

The Anisotropic Yielding Model in ABAQUS[27] requires as input for anisotropic materials the plastic stress – plastic strain data in addition to the yield stress ratios determined from equations (2) and (3). As such, for the S2-Glass/SC-15 tows and yarns, the computed R_{ij}, $i,j = 1, 2, 3$ and the $\bar{\sigma} - \bar{\varepsilon}_p$ data generated from equation (4) are prescribed as input. For isotropic materials on the other hand, the yield function in equation (1) reduces to the von Mises criterion, and as such, only the plastic stress–plastic strain data are required as input. Determining the yield stress of $\sigma_y^M = 12.5\,\text{MPa}$ (see Figure 4(b)) for the SC-15 epoxy, the plastic stress–plastic strain data are computed with the aid of equation (5). The elastic material properties listed in Table 2, together with the above stress–strain data, represent the complete set of input material properties for the elastic–plastic simulations reported in this study. The strength magnitudes of the unidirectional S2-Glass/SC-15 composites listed in Table 2 are used later in this study to develop contour maps of potential failure modes.

Results

Normal and shear stress distributions

The maximum shear force V and bending moment M are given by:

$$V = \frac{P}{2} \tag{6}$$

and

$$M = \frac{PL}{4} \tag{7}$$

The total load, P, in equations (6) and (7) is taken to be the maximum load $P = 7,375\,N$ obtained experimentally.[1,2] The average shear stress τ_{avg}, maximum bending stress σ_b, and average contact stress σ_c are then given by:

$$\tau_{avg} = \frac{P}{2WH} \tag{8}$$

and

$$\sigma_b = \frac{3}{2}\frac{PL}{WH^2} \tag{9}$$

and

$$\begin{aligned} \sigma_c &= \frac{P}{A_c}, \text{ where,} \\ A_c &= 2Wc_{avg} \end{aligned} \tag{10}$$

In equation (10), A_c is the average rectangular contact area between the indenter and the Double Stitched 3D Woven Composite short-beam shear specimen, whereas W and c_{avg} are the width of the specimen (see Figure 1) and the average contact width, respectively. The contact width c is defined as the distance along the X-direction from the YZ-symmetry plane, at which the contact stress between the indenter and the composite specimen falls to zero. The average contact width is then computed as $c_{avg} = \sum_{i=1}^{n_{ep}} c_i/n_{ep}$, wherein n_{ep} is the number of finite element planes along the Y-direction or the number of elements in the Y-direction. In this study, $n_{ep} = 39$, as shown in Figure 3(b).

The stresses reported in this section were computed at the centroids of all the elements in the finite element mesh shown in Figure 3(b). The mechanics of quasi-static indentation are such that the major stresses driving the response are σ_{xx}, σ_{zz}, and τ_{xz} referred to the XYZ coordinate systems established in Figure 3, whereas the stresses σ_{yy}, τ_{xy}, and τ_{yz} referred to the above coordinate systems were found to be negligibly small.

Normalizing the σ_{xx}, σ_{zz}, and τ_{xz} stresses as:

$$\begin{aligned} \hat{\sigma}_{xx} &= \sigma^e_{xx}/\sigma_b \\ \hat{\sigma}_{zz} &= \sigma^e_{zz}/\sigma_c \\ \hat{\tau}_{xz} &= \tau^e_{xz}/\tau_{avg} \end{aligned} \tag{11}$$

serves to better discern the effect of stress concentrations on the mechanics of the Double Stitched 3D Woven Composite. In equation (11), τ^e_{xz}, σ^e_{xx}, and σ^e_{zz} are the stresses at the centroids of each element shown in Figure 3. The normalized stresses in equation (11) are plotted for the Double Stitched 3D Woven Composite, at element centroids, adjacent to the XZ-symmetry plane (see Figure 5(a)) and the XZ-free surface (see Figure 5(b)).

For every finite element column in Figure 5(a), the $\hat{\sigma}_{xx}$ stress is predicted to acquire local maxima in the regions $0.95 < \hat{h} < 1.0$ and $0.0 < \hat{h} < 0.05$, owing to the 0°-oriented Z-Crowns and the bending mechanics of the composite beam. Whereas in the region $0.05 < \hat{h} < 0.95$, $\hat{\sigma}_{xx}$ stresses are significantly lesser, since the local material directions of the Z-yarns are now oriented as shown in Figure 1, resulting in weaker planar stiffness parallel to the global $X-Y$ plane.

However, in Figure 5(b), the $\hat{\sigma}_{xx}$ stress is seen to jump from local minima to local maxima along individual element columns. This is again because of the local architecture comprising of alternating layers of pure matrix and 0°-oriented warp tows. Regardless of the spatial position of the element column as indicated by the parameter $\hat{x}$, the $\hat{\sigma}_{zz}$ stresses in Figure 5(a) and (b) are negligible relative to the $\hat{\sigma}_{xx}$ stresses. As such, further discussions of the $\hat{\sigma}_{zz}$ stresses are eschewed.

Perhaps the most striking results in Figure 5(a) and (b) correspond to the profiles of the $\hat{\sigma}_{xz}$ stresses. The classical elasticity solution for a linear elastic orthotropic beam in three-point bending would predict a parabolic profile of the shear stress with the maximum in the middle. If the peak magnitudes of the $\hat{\sigma}_{xz}$ stresses are joined by a smooth curve, the results are parabolas at various spatial positions, as shown by dotted lines in Figure 5(a) and (b). This result is also consistent with the recent work of Walter et al.[3] For the same location as prescribed by $\hat{x}$, and in the range $0.14 < \hat{h} < 0.86$, the maxima of the $\hat{\sigma}_{xz}$ stresses in Figure 5(a) are lower than those of their counterparts in Figure 5(b), indicating the better reinforcing ability of the Z-yarns. It should be noted herein that this aspect is indicative of material response, since the computed finite element stresses are normalized by the same load P, regardless of their spatial location. The lack of Z-yarns and weaker interfaces between the fill and warp tows and pure matrix and warp tows in the local weave architecture shown in Figure 5(b) leads to higher concentrations of the $\hat{\sigma}_{xz}$ stresses. These results indicate a greater propensity of interfacial crack initiation adjacent to sectional planes with weave architecture resembling the one shown in Figure 5(b).

Motivated by the results for the $\hat{\sigma}_{xz}$ stresses in Figure 5, loci of the locations of the maximum $\hat{\sigma}_{xz}$ stress were computed. These results, shown in Figure 6, for four unique cross-sectional planes along the width (global Y-direction) of the composite beam, exhibit a zone of high inter-laminar $\hat{\sigma}_{xz}$ shear stresses in the region $0.4 < \hat{h} < 0.6$.[3] Based on the maximum $\hat{\sigma}_{xz}$ stress loci, it is hypothesized that potential delamination cracks are likely to initiate in the above-mentioned regions.

Failure modes in quasi-static indentation

In order to understand the implications of the stress fields, contour maps of potential failure modes were constructed. However, it is imperative to first determine which element failed under the induced state of stress. For this purpose, element load factors λ^e_{LF} are

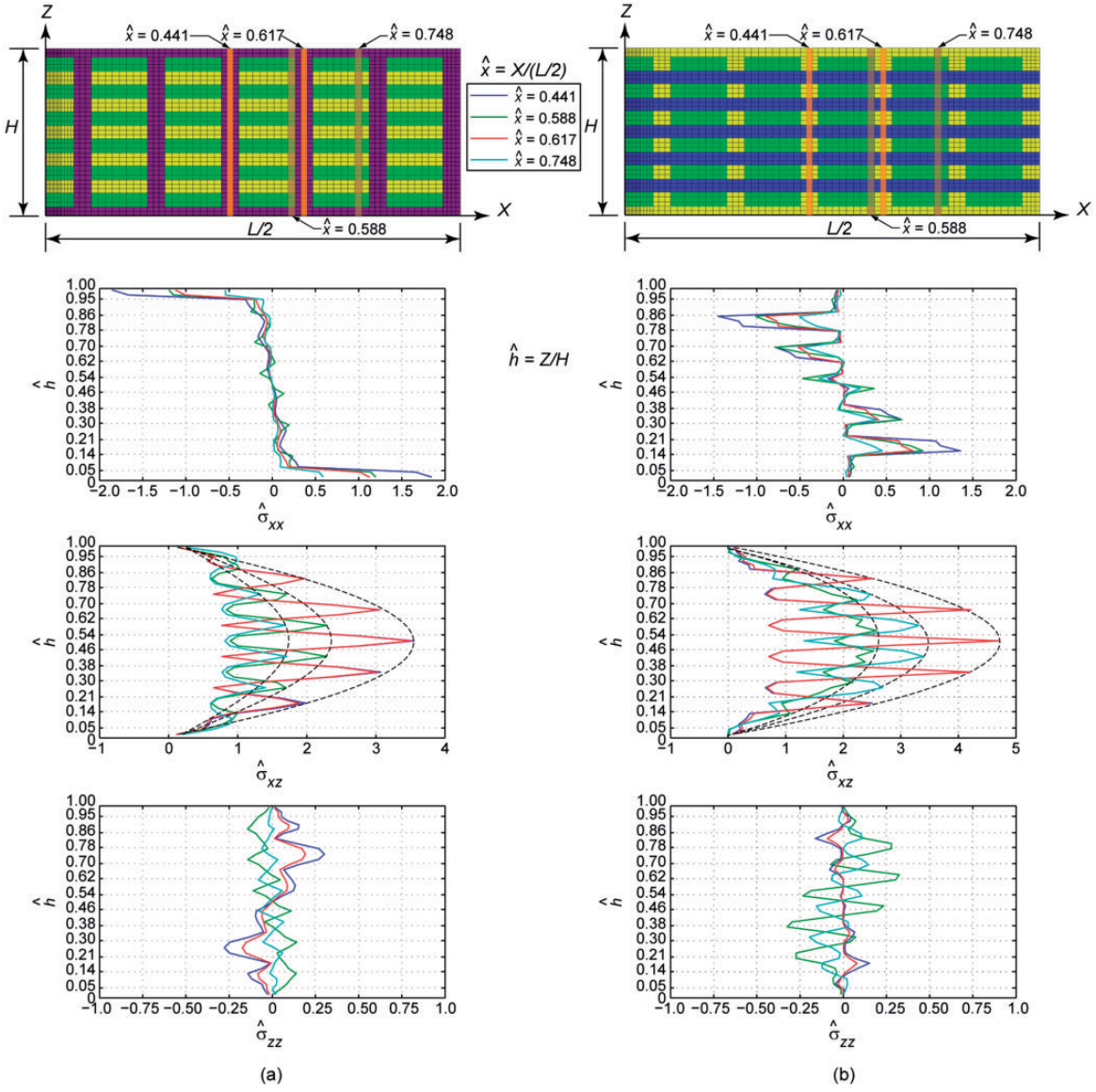

Figure 5. Normal and shear stress profiles adjacent to the *XZ*-symmetry plane and *XZ*-free surface. Column (a): Profiles of the normalized $\hat{\sigma}_{xx}$, $\hat{\sigma}_{xz}$, and $\hat{\sigma}_{zz}$ stresses for the four highlighted element columns adjacent to the *XZ*-symmetry plane, plotted as functions of the normalized panel semi-length $\hat{x}$ and normalized panel height $\hat{h}$. Column (b): Profiles of the normalized $\hat{\sigma}_{xx}$, $\hat{\sigma}_{xz}$, and $\hat{\sigma}_{zz}$ stresses for the four highlighted element columns adjacent to the *XZ*-free surface, plotted as functions of the normalized panel semi-length $\hat{x}$ and normalized panel height $\hat{h}$.

computed based on the Tsai-Hill failure criterion (equation (12)) for the yarn and the maximum principal stress failure criterion (equation (13)) for the matrix:

$$\lambda_{LF}^{e} = \sqrt{\left(\frac{s_{11}^{e}}{X}\right)^{2} - \left(\frac{s_{11}^{e}s_{22}^{e}}{X^{2}}\right) + \left(\frac{s_{22}^{e}}{Y}\right)^{2} + \left(\frac{s_{12}^{e}}{S}\right)^{2}} \quad (12)$$

$$\lambda_{LF}^{e} = MAX\left(\frac{\sigma_{1}^{e}}{S_{y}^{m}}, \frac{\sigma_{2}^{e}}{S_{y}^{m}}, \frac{\sigma_{3}^{e}}{S_{y}^{m}}\right) \quad (13)$$

Failure of an element is determined as follows:

$$\begin{aligned} \lambda_{LF}^{e} < 1 &\Rightarrow \textit{No element failure} \\ \lambda_{LF}^{e} \geq 1 &\Rightarrow \textit{Element failure} \end{aligned} \quad (14)$$

In equation (12), $\{s\}^{e} = \{s_{11}^{e}, s_{22}^{e}, s_{12}^{e}\}$ represents a plane stress state in the 1-2 plane, in a generic element e. On the other hand, in equation (13), $\{\sigma_{p}\}^{e} = \{\sigma_{1}^{e}, \sigma_{2}^{e}, \sigma_{3}^{e}\}$ are the element principal stresses as determined from the element stresses $\{s\}^{e} = \{s_{11}^{e}, s_{22}^{e}, s_{33}^{e}, s_{12}^{e}, s_{13}^{e}, s_{23}^{e}\}$.

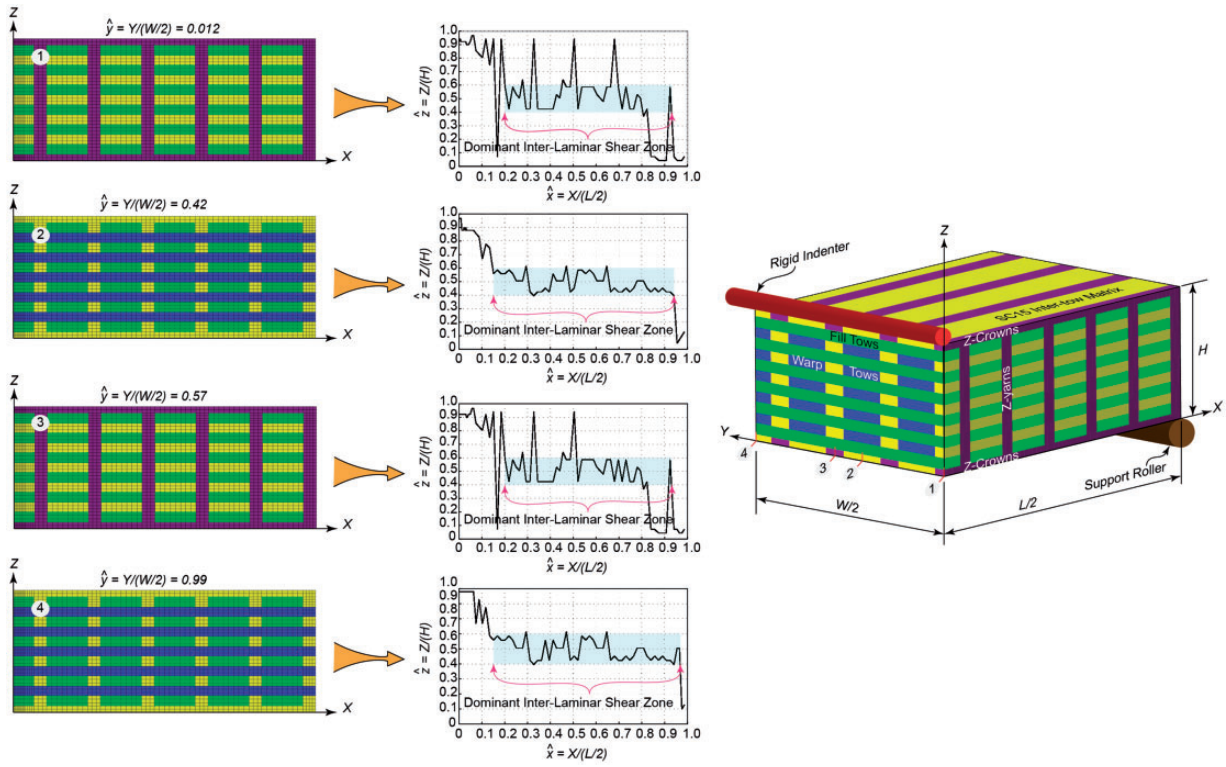

Figure 6. Location of maximum inter-laminar shear stress σ_{xz} at different planes along the width of the short-beam shear specimen. The central inter-laminar shear zones lead to extensive delamination cracking in the Double Stitched 3D Woven Composite panel.

If the element e is determined to reside within a tow, then the stress vector $\{s\}^e$ in equation (12) is appropriately updated for individual material elements viz., warp tows, fill tows, Z-Crowns, and vertical spans of the Z-yarns, by taking into account specific local material directions as illustrated in Figure 1. This is plausible since, in the present case, σ_{xx}, σ_{zz}, and σ_{xz} referred to the global XYZ coordinate system are the only dominant stresses. For the above material elements, the components of $\{s\}^e$ entering into equation (12) are reported in Table 3. This updated stress vector $\{s\}^e$ is now used in conjunction with equation (12) to compute a load factor λ^e_{LF}.

If the element e is determined to reside within the matrix phase, then the 3D stress tensor represented in vector form by $\{s\}^e = \{s^e_{11}, s^e_{22}, s^e_{33}, s^e_{12}, s^e_{13}, s^e_{23}\}$ is used to compute the element principal stress vector $\{\sigma_p\}^e = \{\sigma^e_1, \sigma^e_2, \sigma^e_3\}$. The corresponding load factor λ^e_{LF} for matrix elements is computed from equation (13), wherein the yield strength of the matrix material is computed as:

$$S^m_y = S_{LT} \tag{15}$$

For every failed tow element e^f_t, an auxiliary vector is computed as:

$$\left\{d^f_t\right\} = \begin{Bmatrix} s^e_{11}/X \\ s^e_{22}/Y \\ s^e_{12}/S \end{Bmatrix} \tag{16}$$

The strengths X, Y, and S entering into equation (16) are specified as follows:

$$X = \begin{cases} S^+_L \rightarrow if\, s^e_{11} > 0 \\ S^-_L \rightarrow if\, s^e_{11} < 0 \end{cases} \tag{17a}$$

$$Y = \begin{cases} S^+_T \rightarrow if\, s^e_{22} > 0 \\ S^-_T \rightarrow if\, s^e_{22} < 0 \end{cases} \tag{17b}$$

$$S = S_{LT} \tag{17c}$$

As discussed earlier, the stress vector $\{s\}^e$ in equations (16) and (17) is updated consistent with Figure 1

Table 3. The local stress components to be included while predicting damage initiation. The angles θ_x,θ_y,θ_z are the magnitudes of rotations about the *X*-, *Y*-, and *Z*-axes in Figure 3, respectively.

Material entity	s_{11}	s_{22}	s_{12}	Coordinate rotations
Warp tows	σ_{11}	σ_{33}	τ_{13}	θ_x=0, θ_y=0, θ_z=0
Fill tows	σ_{22}	σ_{33}	τ_{23}	θ_x=0, θ_y=0, θ_z=90
Z-crowns	σ_{11}	σ_{33}	τ_{13}	θ_x=0, θ_y=0, θ_z=0
Z-yarns in through-thickness direction	σ_{11}	σ_{33}	τ_{13}	θ_x=0, θ_y=90, θ_z=0

and Table 3. Furthermore, a scalar parameter d_{max} is then computed as:

$$d_{max} = MAX\left(\left\{d_t^f\right\}\right) \tag{18}$$

Now using d_{max} from equation (18), and information regarding element failure from equations (12)–(15), unique tow/yarn and matrix failure modes are assigned as:

$$f_m = \begin{cases} 0 \Rightarrow No\ Failure \\ 1\ if\ d_{max} = d_t^f(1) \Rightarrow Tow/Yarn\ Longitudianl\ Failure \\ 2\ if\ d_{max} = d_t^f(2) \Rightarrow Tow/Yarn\ Transverse\ Failure \\ 3\ if\ d_{max} = d_t^f(3) \Rightarrow Tow/Inter-Lamainar\ Shear\ Failure \\ 4 \Rightarrow Matrix\ Failure \end{cases} \tag{19}$$

Contour maps of the failure modes determined above are presented for material planes adjacent to the *XZ*-symmetry plane ($\hat{y} = 0.012$), *XZ*-free surface ($\hat{y} = 0.99$), and two intermediate planes ($\hat{y} = 0.42$ and $\hat{y} = 0.57$), in Figure 7. As evident, the contour maps in Figure 7 preserve self-similarity. This self-similarity is attributable to the periodicity in weave architecture and the lack of any appreciable stress gradients in the *Y*-direction.

The *dark blue* patches appearing in the contour maps of Figure 7 correspond to $f_m = 0$, indicating *No Failure*. The *dark blue* patches in Figure 7 are more dominant in Plane 1 and Plane 3 compared with Plane 2 and Plane 4. The weave architecture in Plane 1 and Plane 3 incorporates through-thickness Z-yarns while these are absent in Plane 2 and Plane 4. The difference in weave architecture leads to the stress states presented in Figure 5(a) and (b). As shown in Figure 5(a), the $\hat{\sigma}_{xx}$ stresses are negligible everywhere except near the top and bottom of the specimen, while the $\hat{\sigma}_{xz}$ stresses are appreciable. On the other hand, in Figure 5(b) it is evident that both the $\hat{\sigma}_{xx}$ and $\hat{\sigma}_{xz}$ stresses are of appreciable magnitudes. Therefore, *No Failure* zones corresponding to $f_m = 0$ are abundant at and near Planes 1 and 3 in Figure 7. Z-yarns are known to lower the overall strength by creating damage sites, but help to minimize the spread of damage in the form of delaminations.[25] This aspect would be self-evident in the following discussions.

The *light blue* colored contour patches in Figure 7 correspond to $f_m = 1$, indicating *Tow/Yarn Longitudinal Failure*. The distribution of the *light blue* colored swathes is very sparse since the tows/yarns are stronger in their local *1*-direction (see S_L^+ and S_L^- in Table 2) relative to their local transverse *2*- and *3*-directions. However, the concentration of these *light blue* patches near the top and bottom of the composite specimen (see Plane 1 and Plane 3 in Figure 7) points to the potential initiation of tensile cracks in these regions. These predictions are consistent with the reported profiles of the $\hat{\sigma}_{xx}$ stress in Figure 5(a).

The *light green* colored contour patches in Figure 7 correspond to $f_m = 2$, indicating *Tow/Yarn Transverse Failure*. Note that contour patches of this color cover greater regions in Plane 2 and Plane 4 in comparison with Plane 1 and Plane 3. Once again, the local weave architecture is responsible for the underlying mechanics. At and near Plane 1 and Plane 3, the through-thickness Z-yarns provide a more robust reinforcing effect, than the 0/90 layup at and near Plane 2 and Plane 4. Since the local *1*-direction of the fill tows is aligned with the global *Y*-direction, transverse failure of these tow elements is abundant in Plane 2 and Plane 4. Concentrations of the *light green* colored contour patches near the top and bottom of the composite specimen at Plane 1 and Plane 3 are indicative of the propensity of transverse tensile crack initiation, consistent with the reported profiles of the $\hat{\sigma}_{xx}$ stress in Figure 5(a) and (b).

Tow/Inter − Laminar Shear Failure corresponding to $f_m = 3$ is indicated by the *bright orange* color contours in Figure 7. Almost exclusively, this type of failure is predicted to occur only in Plane 2 and Plane 4 and in the middle bulk of the composite specimen. This result is hardly surprising as the above regions encompass a 0/90 layup architecture for the most part, and it is well known that 0/90 layered composites are highly susceptible to delamination cracking and failure. Furthermore, these results are also consistent with the distributions of the $\hat{\sigma}_{xz}$ stress reported in Figures 6(a)

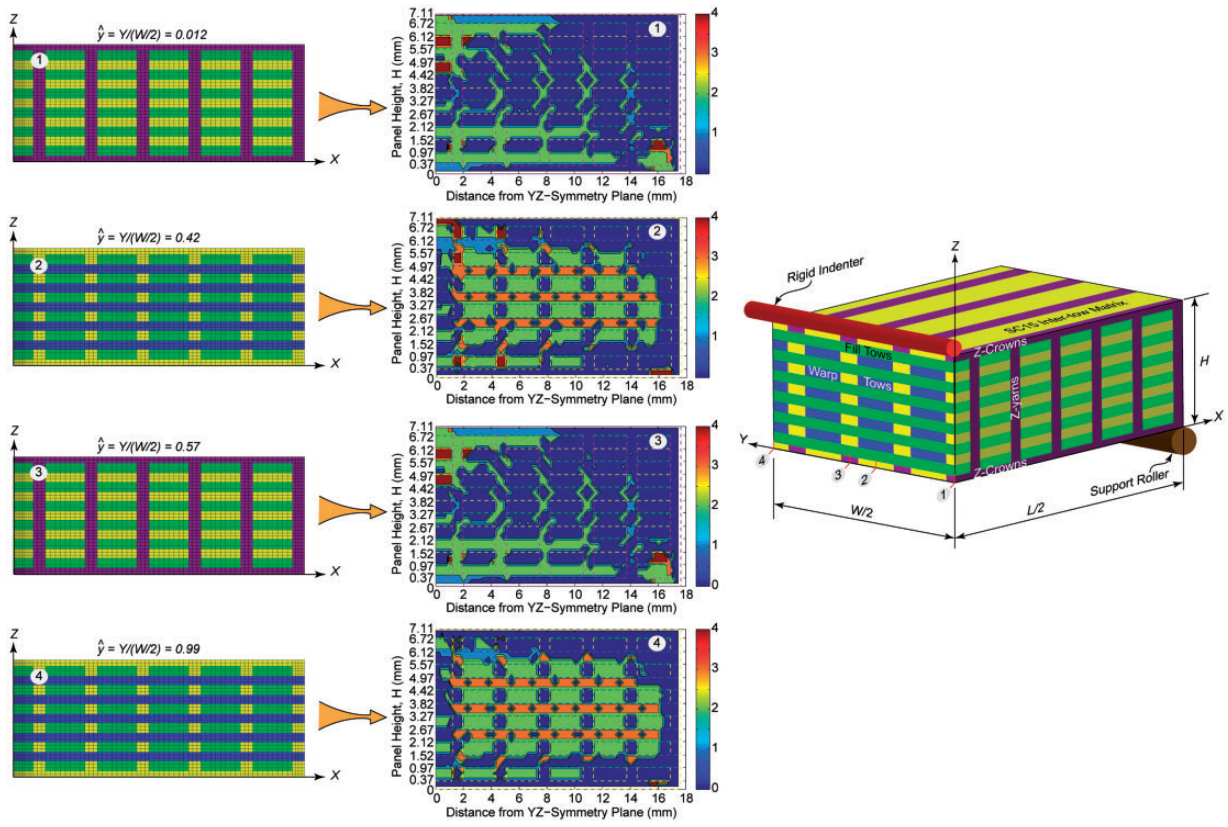

Figure 7. Contour maps of predicted failure modes at unique sectional planes along the width of the Double Stitched 3D Woven Composite specimen. The dotted lines represent the schematics of the local weave architecture. The color bar on the other hand represents numeric values assigned to different failure modes. In particular, 0 → no failure, 1 → tow longitudinal failure, 2 → tow transverse failure, 3 → tow/inter-laminar shear failure, and 4 → matrix failure.

and (b) that exhibit significant concentrations in the inter-laminar regions.

Finally, the *dark red* contour regions in Figure 7 corresponding to $f_m = 4$ indicate *Matrix Failure*. Notice that at Plane 2, matrix failure is predicted to be mostly concentrated near the top of the composite specimen, especially right beneath the indenter. High contact stresses in these regions exceed the yield strength of the matrix leading to considerable crazing.[7] However, due to free surface effects, the same region of composite specimen at Plane 4 does not experience any matrix failure at all. Also at Plane 1 and Plane 3, matrix failure is mostly predicted near the top of the composite specimen, within a volume influenced by the action of the rigid indenter.

Micrographs of damage

Post-failure sectioned micrographs of damage in the current composite specimen are shown in Figure 8. These micrographs were first reported by Walter et al.[1,2] For the sake of reference, a schematic of the indenter is also positioned in Figure 8. The evident asymmetry of the two micrographs in Figure 8 is a post-processing artifact, and does not indicate poor quality of the tested specimens.

At the outset, it should be mentioned that the highlighted large-scale damage is processing-induced and not a result of experimentation. All the other discernible cracks were initiated and propagated as a result of quasi-static indentation. The two micrographs were obtained upon appropriately sectioning and polishing failed specimens such as to include through thickness Z-yarns (see Figure 8(a)) and to exclude the same (see Figure 8(b)).

Comparing the micrograph and the corresponding contour map of predicted failure modes for Plane 3, as shown in Figure 8(a), some similarities and differences are apparent. Firstly, the contour map for Plane 3 predicts transverse tow cracking near the top and bottom of the composite specimen. This is clearly evident in the micrograph of Figure 8(a). Cracks 1–4 in Figure 8(a) are predominantly interfacial cracks, but this is not predicted by the contour map at Plane 3. However, some transverse tow cracking is indeed predicted at Plane 3 at locations approximately

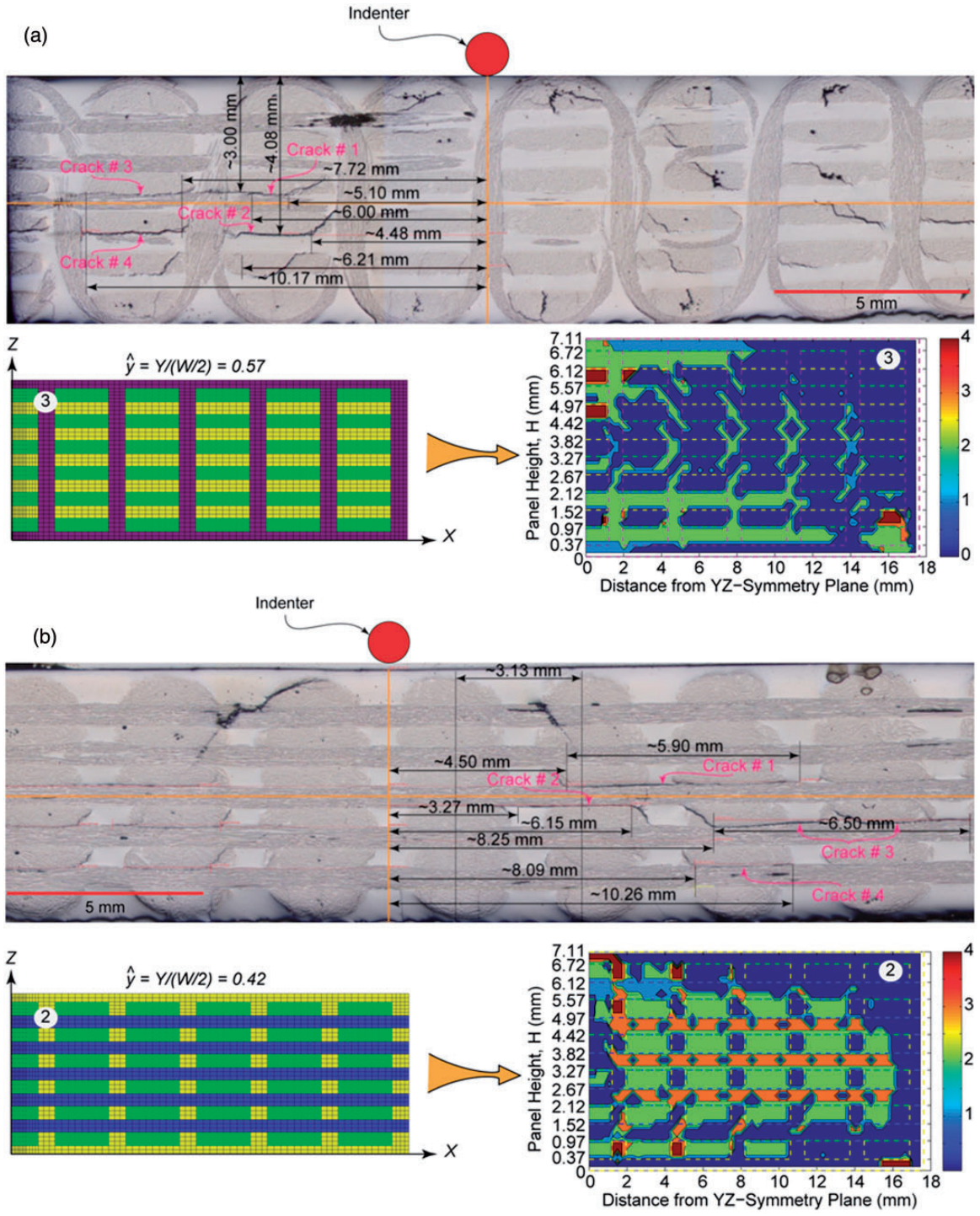

Figure 8. Experimental validation of inter-laminar delamination cracks in the Double Stitched 3D Woven Composite panel. (a) Micrograph exhibiting delamination damage at a section of the specimen comprising through-thickness Z-yarns. The corresponding finite element mesh and predicted failure modes contour maps are also shown below the micrograph. (b) Micrograph displaying delamination cracks at the section between two consecutive Z-yarns. The corresponding finite element mesh and predicted failure modes contour maps are also shown below the micrograph.

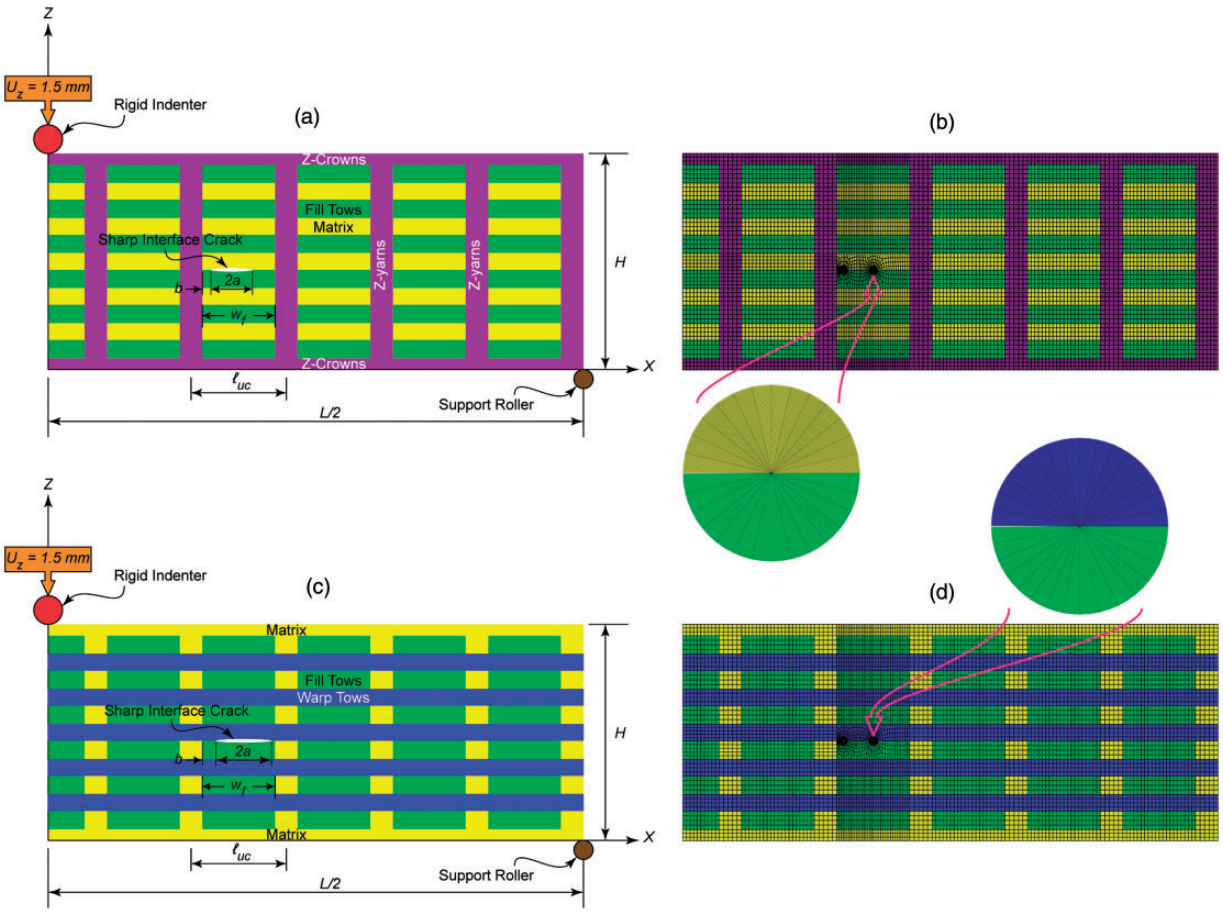

Figure 9. 2D plane strain representations of the quasi-static indentation problem addressed in this study. (a) 2D schematic representation of the weave architecture of Plane 1 in Figure 8 showing the location of a sharp interface crack of length, *2a*. (b) The corresponding finite element mesh constructed with 2D 8-noded isoparametric plane strain elements. Quarter-point singularity elements are used in the pulled-out near-tip region. (c) 2D schematic representation of the weave architecture of Plane 2 in Figure 8 showing the location of a sharp interface crack of length, *2a*. (d) The corresponding finite element mesh discretized with 2D 8-noded isoparametric plane strain elements. A zoomed-in view of the near-tip region comprising of quarter-point singularity elements is also presented.

corresponding to those of Cracks1–4 in Figure 8(a). More importantly, these cracks in Figure 8(a) do not seem to go through the Z-yarns, thereby demonstrating that the Z-yarns are effective crack shields, as also reported by Seltzer et al.[25]

The micrograph in Figure 8(b) incorporates several interface cracks of which Cracks1–4 have been labeled with dimensions. The unique attribute of these cracks is that they span multiple tow widths unlike the cracks in Figure 8(a) that were confined to one tow width. This physical observation implies that the absence of through-thickness Z-yarns facilitates interfacial delamination and crack propagation. With this background, if we now look at the contour map at Plane 2 reproduced in Figure 8(b), the consistency of the predictions regarding the locations and extents of the interfacial delamination with their experimental counterparts becomes evident.

It would be remiss not to mention that the location of the rigid indenter might play an important role in influencing the mechanics of the composite specimens under consideration. In all the simulations reported herein, the indenter is placed such that both tow and matrix elements come in contact with the same and symmetry conditions are maintained. However, in experiments, it is difficult to accurately control the position of the indenter and by extension the line of contact. Based upon analyses of several different micrographs of damage, it is surmised that the location of the indenter is most likely as that shown in Figure 8.

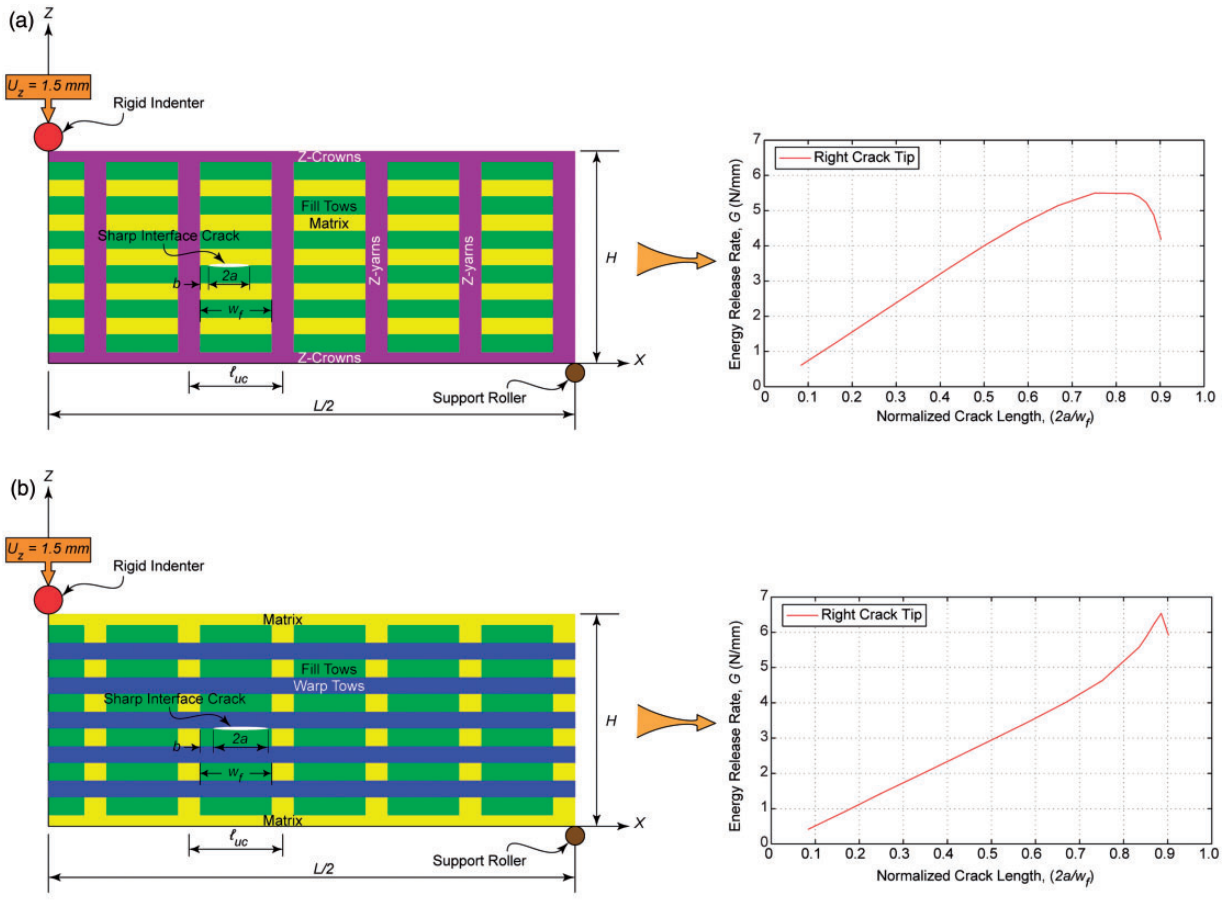

Figure 10. Strain energy release rate $\mathcal{G}$ as a function of normalized crack length. (a) In Configuration # 1, $\mathcal{G}$ suddenly *decreases* in close proximity to the Z-yarn exhibiting its significant crack shielding abilities. (b) In Configuration # 2, $\mathcal{G}$ suddenly *increases* in close proximity to the tri-material junction comprised of warp tows, fill tows, and matrix material. As such, the crack could potentially propagate unimpeded.

This discrepancy may also explain some of the observed differences between finite element predictions and experimental observations.

Overall, it could be argued that the results reported in Figure 8 validate the hypothesis regarding dominant interlaminar shear failure in the middle ($0.4 < \hat{h} < 0.6$) of the composite specimen in between two successive Z-yarns. Near the vicinities of the through-thickness reinforcements, however, the above failure modes are effectively resisted by the reinforcing effects provided by the Z-yarns.

Linear elastic fracture mechanics analysis

The intent of this section is to understand the interaction of the through-thickness Z-yarns with interfacial delamination cracks. Once again looking back at the micrographs in Figure 8, it is evident that the symmetry conditions exploited in finite element modeling are not strictly observed in practice. Therefore, a fully 3D finite element model incorporating progressive material damage might be needed to gain detailed insight into the mechanics of the current composite specimen under quasi-static indentation. Nevertheless, a fundamental, qualitative assessment of the role of Z-yarns could be made by developing equivalent 2D plane strain finite element models incorporating an interfacial crack and computing the mixed-mode strain energy release rate, $\mathcal{G}$, as a function of the crack length.

2D plane strain models

As discussed in previous sections and shown in Figures 6–9, the current Double Stitched 3D Woven Composite specimen is comprised of two unique cross-sectional weave architectures. It is clearly evident from the micrographs in Figure 8 that delamination cracks appear to initiate approximately one unit-cell away from the location of the indenter. Taking these two crucial observations into account, 2D plane strain finite element models incorporating an interfacial crack are developed as shown in Figure 9.

Figure 9(a) shows a schematic of the weave architecture incorporating through-thickness Z-yarns and a delamination crack modeled as a sharp crack of length, $2a$. This arrangement is referred to as Configuration # 1. The corresponding finite element mesh of Configuration # 1 is shown in Figure 9(b). On the other hand, a schematic of the weave architecture omitting the through-thickness Z-yarns, while incorporating the 0°-oriented warp tows, the 90°-oriented fill tows, the matrix material, and a delamination crack modeled as a sharp crack of length, $2a$, is shown in Figure 9(c). This arrangement is referred to as Configuration # 2. The finite element mesh of Configuration # 2 is reported in Figure 9(d). Figure 9(b) and (d) also include a zoomed-in view of the near-tip region exhibiting local mesh refinements to adequately capture the stress singularity. This is achieved with the aid of quarter-point singularity elements in the first ring of elements around the crack tip. In Configuration # 1 (see Figure 9(b)), the mesh comprises of a total of 12,373 elements, and 36,107 nodes resulting in 69,060 degrees of freedom. In Configuration # 2, (see Figure 9(d)), the mesh comprises of a total of 11,886 elements and 34,670 nodes resulting in 66,234 degrees of freedom.

The rigid indenter and support rollers are located as shown in Figure 9(a) and (c). Appropriate contact conditions are established between the indenter and top surface and the support roller and the bottom surface of the composite specimen. The crack surfaces are traction-free, but contact conditions are also established at these surfaces using the built-in general contact algorithm in ABAQUS.[27] As before, the indenter is displaced in the negative Z-direction: $U_z = 1.5\,mm$.

In this modeling effort, the S2-Glass/SC15 tows/yarns are modeled as transversely isotropic linear elastic materials, while the SC15 matrix phase is specified to be an isotropic linear elastic material. The properties of these two material systems are reported in Table 2.

Computing the strain energy release rate, $\mathcal{G}$

The interfacial cracks in the finite element models shown in Figure 9(b) and (d) comprise of two crack tips. The Left Crack Tip (LCT) is closer to the indenter, while the Right Crack Tip (RCT) is farther away. In the simulations reported herein, the LCT is held fixed in its location, whereas the RCT is propagated outward in the positive X-direction. In Configuration # 1 and Configuration # 2 a total of 14 simulations were performed by successively incrementing the crack length.

Since the tow/yarn and matrix materials are linear elastic in these simulations, the strain energy release rate, $\mathcal{G}$, is computed as the contour J-integral around the crack tip. The J-integral is evaluated at five contours around each crack tip, wherein the first contour is closest to the crack tip and the others are successively farther away. Owing to potential inaccuracy of results for stresses in the singular region near the crack tip, the J-integral from the first contour evaluation is neglected and the strain energy release rate is computed as:

$$\mathcal{G} = \left[\frac{\sum_{i=2}^{n} J_i}{(n-1)}\right],\ n = 5 \tag{22}$$

The average strain energy release rate, $\mathcal{G}$, computed using equation (22) is shown in Figure 10(a) and (b) for Configuration # 1 and Configuration # 2, respectively.

Effect of Z-yarns

As shown in Figure 10(a), the strain energy release rate, $\mathcal{G}$, for the RCT increases in the range $0.0 < \frac{2a}{w_f} \leq 0.75$, since an effective crack arresting medium or entity is absent. Further crack propagation in the range $0.83 < \frac{2a}{w_f} \leq 0.90$ results in a sudden and drastic decrease in the strain energy release rate, $\mathcal{G}$, for the RCT. Note that the local material directions of the through-thickness Z-yarns are oriented such that their *1*-direction (aligned parallel to the global Z-direction) is orthogonal to the direction of crack propagation. As such, the crack continuously approaches a stiffer barrier in the range $0.83 < \frac{2a}{w_f} \leq 0.90$. Consequently, the sudden and drastic decrease in the strain energy release rate, $\mathcal{G}$, for the RCT in the above range is a manifestation of the crack shielding effect provided by the Z-yarns.

Let us look back at the micrograph in Figure 8(a). The labeled cracks in particular do appear to kink as they approach the Z-yarns and deflect parallel to them. Even the other visible cracks in Figure 8(a) do seem to incorporate an interfacial segment, although some of them kink and traverse through the tows much before they approach the nearest Z-yarn. This response could be an artifact of the local stress state in those regions that might, for instance, promote transverse tow cracking over interfacial delamination.

On the other hand, the strain energy release rate, $\mathcal{G}$, of the RCT in Configuration # 2 accelerates in the range $0.75 < \frac{2a}{w_f} \leq 0.83$, as shown in Figure 10(b). Furthermore, $\mathcal{G}$, of the RCT in Configuration # 2 remains greater than that in Configuration # 1 within the range $0.83 < \frac{2a}{w_f} \leq 0.90$, as also shown in Figure 10(b). These observations lead one to surmise that inter-laminar cracks between two consecutive Z-yarns do not experience an effective barrier against propagation. Consequently, it is to be expected that crack lengths in these regions would be longer than in the

vicinities of Z-yarns, as confirmed by the micrograph in Figure 8(b).

Based on the above analysis, the natural deduction would be to recommend minimal spacing between individual Z-yarns. However, such recommendations have to be evaluated in the context of other parameters such as in-plane and out-of-plane stiffness and strength,[8] performance under impact loading conditions, and perhaps conformability to near-net-shape manufacturing.

Conclusions

Detailed finite element models were developed to investigate the quasi-static indentation mechanics of S2Glass/SC15 3D woven composites. Plasticity-driven crazing damage of the matrix material was only observed in the vicinity of the indenter. Experimental evidence supports the notion that significant inter-layer delamination and transverse tow cracking are chiefly responsible for the observed softening response of S2Glass/SC15 3D woven composites under quasi-static indentation.

Stress analysis in the through-thickness direction predicted inter-laminar shear stress concentrations of magnitudes up to 4.5 times the average shear stress. These high stress concentrations were shown to result in zones of dominant inter-laminar shear within the range $0.4 \leq \hat{h} \leq 0.6$, wherein $\hat{h} = Z/H$ is the normalized thickness of the specimen tested. Sectioned micrographs of damaged specimens revealed that most inter-laminar cracks were indeed located within the zones of dominant inter-laminar shear.

Novel contour maps of failure modes in S2Glass/SC15 3D woven composites under quasi-static indentation were developed on the basis of computed stresses in the through-thickness direction. These contour maps also indicate significant propensity for inter-laminar shear delaminations within the range $0.4 \leq \hat{h} \leq 0.6$, especially between two consecutive Z-yarns. Equivalent 2D plane strain fracture mechanics models juxtaposed with experimental evidence and contour maps of failure modes clearly bring to light the ability of Z-yarns to effectively shield inter-laminar cracks.

Acknowledgements

The authors would also like to thank Dr Ryan L. Karkkainen at ARL for his insightful comments that helped us improve upon the work. Furthermore, constructive criticism offered by the two anonymous reviewers is greatly appreciated.

Funding

The funding for this work was provided by the United States Army Research Office (Grant number W911NF-08-1-0120), with Dr Bruce LaMattina as the Program Manager and the United States Army Research Laboratory (ARL). The authors are grateful for the financial support.

Conflict of Interest

None declared.

References

1. Walter TR, Subhash G and Sankar BV. In: *CD proceedings of the 24th annual technical meeting of the American Society of Composites*, 15–17 September 2009, Newark. pp.302–308. Lancaster, PA: DEStech Publications, Inc.
2. Walter TR, Subhash G, Sankar BV, et al. Monotonic and cyclic short beam shear response of 3D woven composites. *Compo Sci Technol* 2010; 70: 2190–2197.
3. Walter TR, Subhash G, Sankar BV, et al. A novel method for dynamic short-beam shear testing of 3D woven composites. *Exp Mech* 2013; DOI 10.1007/s11340-012-9659-4).
4. Pankow M, Salvi A, Waas AM, et al. Resistance to delamination of 3D woven textile composites evaluated using end notch flexure (ENF) tests: experimental results. *Composites Part A* 2011; 42: 1463–1476.
5. Pankow M, Waas AM, Yen CF, et al. Resistance to delamination of 3D woven textile composites evaluated using End Notch Flexure (ENF) tests: cohesive zone based computational results). *Composites Part A* 2011; 42: 1863–1872.
6. Rao MP, Sankar BV and Subhash G. Effect of Z-Yarns on the stiffness and strength of three-dimensional woven composites. *Composites Part B* 2009; 40: 540–551.
7. Rao MP, Sankar BV, Subhash G, et al. Modeling quasi-static indentation of 3D woven composites. In: *CD proceedings of the 24th technical conference of the American Society for Composites*, 15–17 September 2009, Newark. pp.211–234. Lancaster, PA: DEStech Publications, Inc.
8. Karkkainen RL and Tzeng JT. Micromechanical strength modeling and investigation of stitch density effects on 3D orthogonal composites. *J Compos Mater* 2009; 43: 3125–3142.
9. Bogdanovich AE. Multi-scale modeling, stress and failure analyses of 3-D woven composites. *J Mater Sci* 2006; 41: 6547–6590.
10. Cox BN. Delamination and buckling in 3D composites. *J Compos Mater* 1994; 28: 1114–1126.
11. Cox BN and Dadkhah MS. The macroscopic elasticity of 3D woven composites. *J Compos Mater* 1995; 29: 785–819.
12. Cox BN, Dadkah MS and Morris WL. On the tensile failure of 3D woven composites. *Composites Part A* 1996; 27: 447–458.
13. Cox BN, Carter WC and Fleck NA. A binary model of textile composites: I formulation. *Acta Metall Mater* 1994; 42: 3463–3479.
14. Xu J, Cox BN, McGlockton MA, et al. A binary model of textile composites: II the elastic regime. *Acta Metall Mater* 1995; 43: 3511–3524.
15. McGlockton MA, Cox BN and McMeeking RM. A binary model of textile composites: III high failure

strain and work of fracture in 3D weaves. *J Mech Phys Solids* 2003; 51: 1573–1600.
16. Naik NK, Azad NMSk and Durga PP. Stress and failure analysis of 3D orthogonal interlock woven composites. *J Reinf Plast Compos* 2001; 20: 1485–1523.
17. Tan P, Tong L, Steven GP, et al. Behavior of 3D orthogonal woven CFRP composites. Part II. FEA and analytical modeling approaches. *Composites Part A* 2000; 31: 273–281.
18. Gama BA, Haque MdJ, Gillespie JW Jr., et al. In: *CD proceedings of 49th international SAMPE symposium and exhibition*, 16–24 May 2004. Long Beach, CA: SAMPE Publication.
19. Baucom JN and Zikry MA. Evolution of failure mechanisms in 2D and 3D woven composites under quasi-static perforation. *J Compos Mater* 2003; 37: 1651–1674.
20. Bahei-El-Din YA and Zikry MA. Impact-induced deformation fields in 2D and 3D woven composites. *Compos Sci Technol* 2003; 63: 923–942.
21. Lv L and Gu B. Transverse impact damage and energy absorption three-dimensional orthogonal hybrid woven composite: experimental and FEM simulation. *J Compos Mater* 2008; 42: 1763–1786.
22. Grogan J, Tekalur SA, Shukla A, et al. Ballistic resistance of 2D and 3D woven sandwich composites. *J Compos Mater* 2007; 9: 283–302.
23. Gong JC and Sankar BV. Impact properties of three-dimensional braided graphite/epoxy composites. *J Compos Mater* 1991; 25: 715–731.
24. Herb V, Martin E and Couégnat G. Damage analysis of thin 3D-woven SiC/SiC composite under low velocity impact loading. *Composites Part A* 2012; 43: 247–253.
25. Seltzer R, González C, Muñoz R, et al. X-ray microtomography analysis of the damage micromechanisms in 3D woven composites under low-velocity impact. *Composites Part A* 2013; 45: 49–60.
26. Pankow M, Salvi A, Waas AM, et al. Split Hopkinson pressure bar testing of 3D woven composites. *Compos Sci Technol* 2011; 71: 1196–1208.
27. ABAQUS® Standard User's Manual, Version 6.9-1. Dassault Systemes Americas Corp., Waltham, MA.
28. Ansar M, Wang X and Zhou C. Modeling strategies for 3D woven composites: A review. *Compos Struct* 2011; 98: 1947–1963.
29. Advanced materials: solutions for demanding applications, South Carolina, USA: AGY, Inc, Aiken. http://www.agy.com/technical_info/graphics_PDFs/Advanced_Materials.pdf (accessed 12 May 2013).
30. SC-15. Toughened Epoxy Resin System data sheet. Applied Poleramic, Inc., Benicia, CA, 2009.
31. Chamis CC, Handler LM and Manderscheid J. Composite nanomechanics: a mechanistic properties prediction. NASA/TM—2007-214673. Cleveland, OH: Glenn Research Center.
32. Hill R. *The mathematical theory of plasticity*. London, UK: Oxford University Press, 1950.
33. Sun CT and Chen JL. A simple flow rule for characterizing nonlinear behavior of fiber composites. *J Compos Mater* 1989; 23: 1009–1020.
34. Xie M and Adams DF. A plasticity model for unidirectional composite materials and its applications in modeling composites testing. *Compos Sci Technol* 1995; 54: 11–21.
35. Zhou Y, Rahman A, Sajedur J, et al. Nonlinear constitutive equation for vapor-grown carbon nonafiber-reinforced SC-15 epoxy at different strain rate. *Mater Sci Eng A* 2007; 465: 238–246.